Journal of Structural Geology 31 (2009) 104–113

Contents lists available at ScienceDirect

Journal of Structural Geology

journal homepage: www.elsevier.com/locate/jsg

Finite strain analysis of a natural ductile shear zone in limestones: Insights into 3-D coaxial vs. non-coaxial deformation partitioning

Stefano Vitale*, Stefano Mazzoli

Dipartimento di Scienze della Terra, Università degli studi di Napoli 'Federico II', Largo San Marcellino 10, 80138 Napoli, Italy

ARTICLE INFO

Article history:
Received 14 April 2008
Received in revised form
10 October 2008
Accepted 26 October 2008
Available online 6 November 2008

Keywords:
General shear
Strain localization
Simple shear
Lateral extrusion
Southern Apennines

ABSTRACT

In order to obtain new insights into the process of strain localization, a ca. 50 m thick shear zone has been investigated. The shear zone, located in the footwall to a major thrust, involves limestones and pelites. Calc-mylonites are characterized by a stretching lineation orthogonal to the shear direction and a foliation at an angle of 45–10° to the thrust fault. Strain analysis and mean foliation analysis have been carried out on 42 samples. Strain gradients and ellipsoid shape across the shear zone indicate, respectively, an increase of strain intensity approaching the thrust surface and overall oblate strain. Apparent flattening increases significantly for intensely deformed rocks. Theoretical models are proposed to explain the recorded finite strain configuration with a main deformation characterized by simultaneous simple shear and localized pure shear involving lengthening normal to the shear direction. A model of asymmetric lateral extrusion is adopted, as is consistent with measured horizontal strain gradients. This model also takes into account regional geological constraints such as the occurrence of accommodation space along the present-day Tyrrhenian extensional margin to the SW, and of a massive body of platform carbonates—forming a rigid buttress—to the NE.

1. Introduction

Heterogeneous ductile shear zones result from simple shear deformation with or without pure shear and volume change components, with at least one of them being characterized by variable intensity (Fossen and Tikoff, 1993; Srivastava et al., 1995; Ring, 1998; Baird and Hudleston, 2007; Horsman and Tikoff, 2007; Vitale and Mazzoli, 2008). Pure shear and volume change components can act synchronously and be localized within the shear zone, or may be distributed into the whole rock volume (Fossen and Tikoff, 1997). The finite configuration of the deformation can be described by an ensemble of geometric measurable quantities such as foliation and lineation attitudes, finite strain ellipticity and shear strain, their gradients across the shear zone and by means of these quantities, assuming that the finite configuration records of the whole deformation history (Hull, 1988; Means, 1995; Horsman and Tikoff, 2007), it is possible to define the main characteristics of the deformation. The path outlined by the correlation between two of these measurable quantities, such as finite strain and the angle between the foliation and the shear plane, is generally referred to as strain path and can provide information on the deformation history (Vitale and Mazzoli, 2008).

Ramsay and Graham (1970) firstly provided a model for a shear zone showing parallel, planar boundaries, characterized by a combination of simple shear and volume change. A pure shear component was taken into account only if homogenously distributed within the whole rock volume, as the presence of a localized pure shear component would produce strain incompatibility between the deformed zone and its wall rock or between different homogeneously deformed portions ('cream cake effect'; Ramsay and Huber, 1987). Subsequently several studies invoked the synchronous occurrence of simple shear, pure shear and volume change to explain natural heterogeneous shear zones (Srivastava et al., 1995; Ring, 1998; Baird and Hudleston, 2007; Horsman and Tikoff, 2007). This simultaneous combination has been modelled by Fossen and Tikoff (1993).

In this study we show how an accurate 3-D analysis of finite strain may provide significant information on the main features of the deformation. The analyzed structures crop out in the Maratea area of the southern Apennines (Fig. 1). The protolith is a sedimentary calcareous succession, characterized by strain markers such as oncoids, ooids, peloids and intraclasts useful to determine finite strain ellipticity. Ductile deformation occurred at very low-grade conditions (Vitale et al., 2007b).

2. Geological setting

The mylonitic shear zone analyzed in this study (Maratea shear zone) is located in the footwall to a major Apennine thrust in

* Corresponding author. Tel.: +39 081 253 8124; fax: +39 081 552 5611.
E-mail address: stvitale@unina.it (S. Vitale).

0191-8141/$ – see front matter © 2008 Elsevier Ltd. All rights reserved.
doi:10.1016/j.jsg.2008.10.011

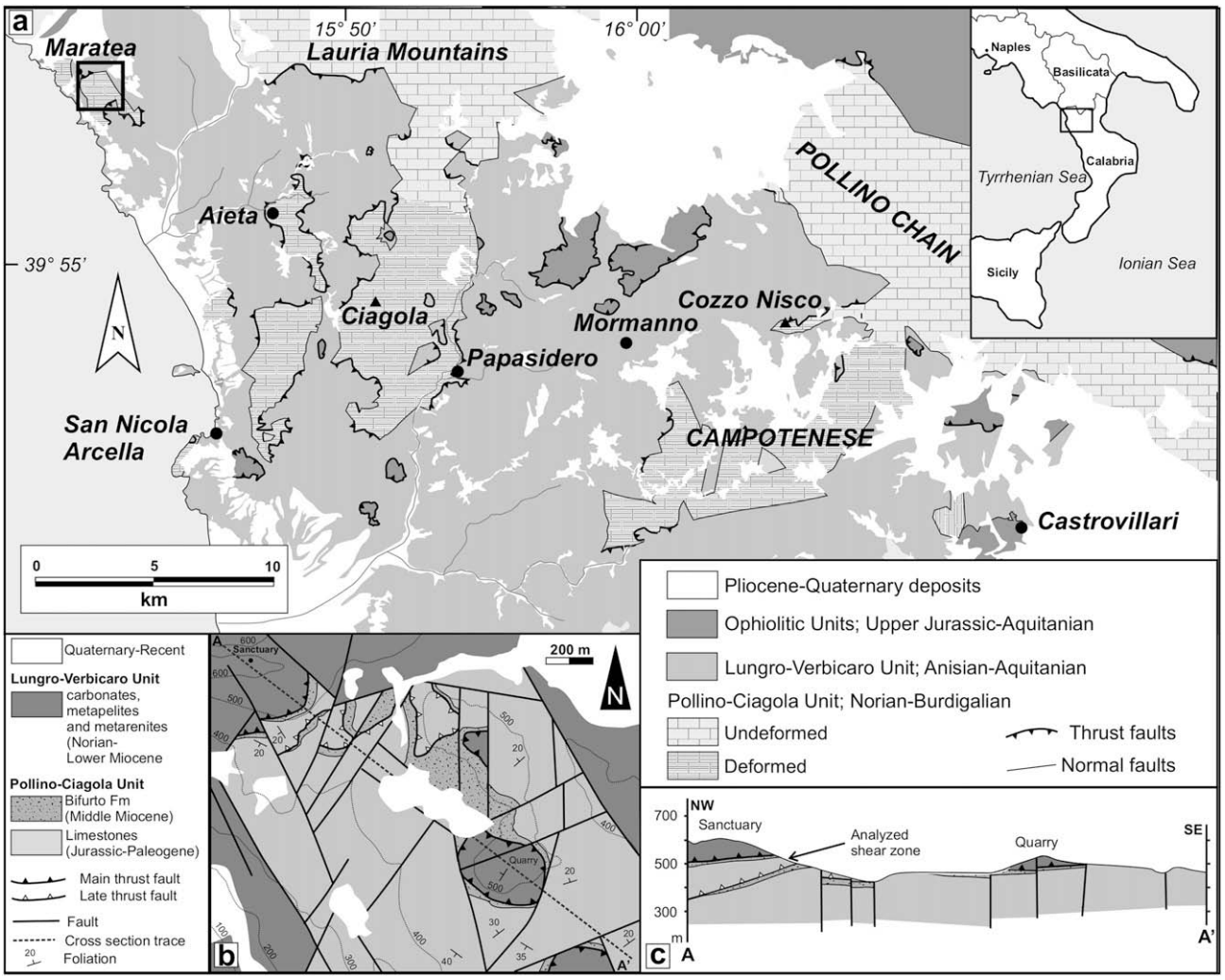

Fig. 1. (a) Tectonic sketch map of the Calabria-Basilicata border area, showing outcrop extent of the Pollino-Ciagola Unit (of which the study area occupies the NW sector). (b) Geological sketch map of the study area. (c) Geological cross section (refer to diagram b for location and legend).

southern Italy (Fig. 1). In this area, a Middle Triassic–Lower Miocene siliciclastic and carbonate metasedimentary succession (Lungro-Verbicaro Unit; Iannace et al., 2007) tectonically overlies an unmetamorphosed Upper Triassic to Middle Miocene succession (Pollino-Ciagola Unit). This latter succession is formed by platform dolomites and limestones (Lauria Mountains and Pollino Chain in Fig. 1a) laterally passing to the SW (Maratea, Aieta, Monte Ciagola, Papasidero and Campotenese areas in Fig. 1a) to carbonate slope-facies limestones. Lower to Middle Miocene siliciclastic rocks of the Bifurto Fm overlay both successions. Thrusting occurred in Middle–Late Miocene times (Iannace et al., 2007). The analyzed shear zone is located SW of the Maratea village (Fig. 1b). In this area, the Pollino-Ciagola Unit crops out within a tectonic window, in the footwall to the major thrust contact. In the northern sector of the area, a deeper thrust fault produced imbrication of the footwall succession, leading the superposition of Mesozoic limestones onto the Bifurto Fm (Fig. 1c).

3. The Maratea shear zone

The carbonate succession of the Pollino-Ciagola Unit is affected by heterogeneous ductile deformation accommodated by several tens to a few hundred metres thick, bedding-parallel shear zones. The uppermost shear zone, analyzed in this study, is located in Cretaceous-Miocene limestones and pelites. In this area the hanging wall is constituted by the Norian to Lower Miocene succession of the Lungro-Verbicaro Unit. In the footwall, immediately below the thrust surface, a discontinuous, several centimetres- to few metre-thick layer of pelites and sandstones of the Bifurto Fm occurs (Fig. 1c).

The studied shear zone is characterized by weakly deformed rocks at the base, progressively grading to intensely deformed rocks close to the thrust surface. It is possible to subdivide the calcareous rocks within the shear zone into three main classes according to rock texture, deformation microstructures and finite strain (Vitale et al., 2007b): (i) weakly deformed limestones (protomylonites), showing prevailing, apparently deformation-free, micritic grains and sparry calcite crystals generally affected by straight twins and deformation bands (Fig. 2a); (ii) moderately to highly deformed micritic rocks (mylonites), displaying few large crystals affected by bent twins characterized by subgrains along microshear or old twin planes (Fig. 2b,c); and (iii) very highly deformed rocks (ultra-mylonites) characterized by rare large grains showing large aspect ratios (*ribbon calcite*) parallel to the main foliation and embedded in a predominantly micritic matrix (Fig. 2d). Optical and electronic (SEM and TEM) microscope investigations have outlined how, for the original micritic component (grain size <5 μm), grain boundary sliding, secondarily accommodated by dislocation creep, was the main deformation mechanism, whereas for the original sparry calcite (grain size >5 μm) mechanical twinning, dislocation creep,

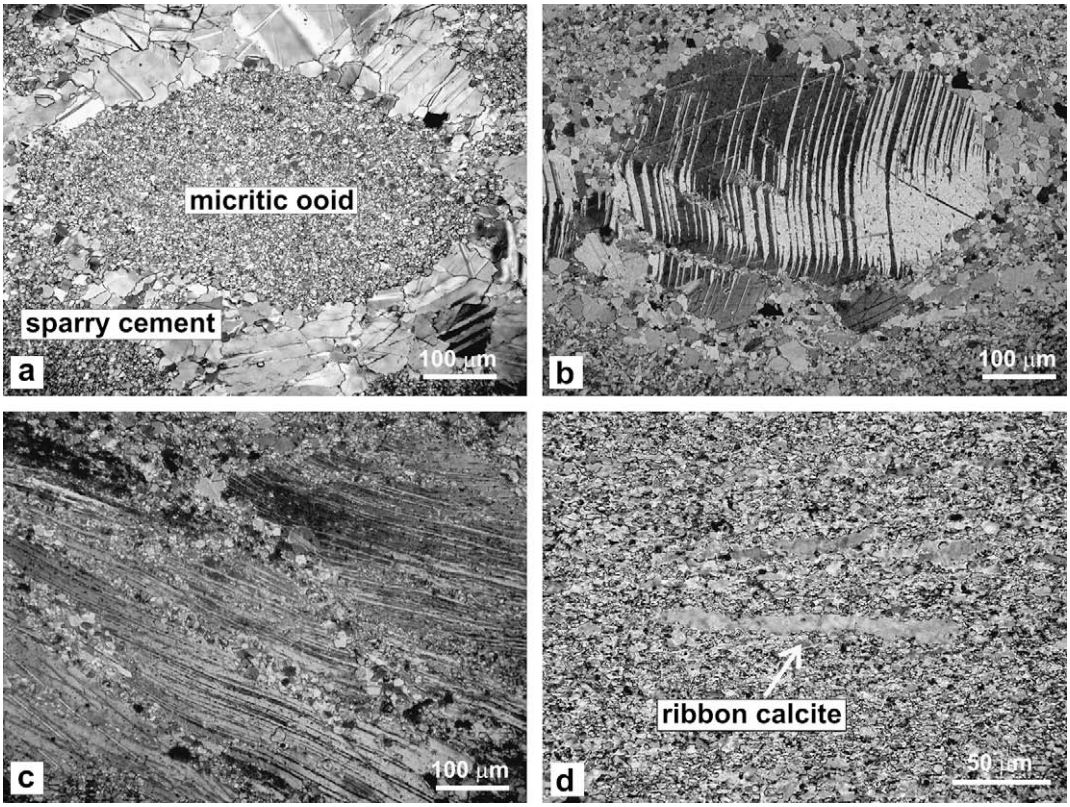

Fig. 2. Microphotographs of deformed rocks within the Maratea shear zone (crossed polars). (a) Protomylonite, showing weakly deformed micritic ooid embedded in sparry cement characterized by straight twinning. (b) Mylonite displaying a large crystal affected by bent twins and subgrains along microshear planes. (c) Highly deformed mylonite consisting of large sparry calcite with deformed twin lamellae and subgrains along shear planes. (d) Ultramylonite characterized by isolated calcite crystals showing large aspect ratio (ribbon calcite), embedded in a micritic matrix.

pressure-solution and dynamic recrystallization were the driving processes (Vitale et al., 2007b). All structures are consistent with sub-greenschist facies conditions for the deformation, which took place at temperatures not exceeding 250 °C (Vitale et al., 2007b).

The analyzed rock types are characterized by variable combinations of deformation intensity and concentration of competent objects embedded in a more or less competent matrix (Fig. 3a–d). At several locations, competent clasts show an asymmetric shape indicating a top-to-the-ESE sense of shear (Fig. 3e,f).

4. Structural analysis

In order to investigate the 3-D finite strain distribution across the Maratea shear zone, foliation and lineation have been measured along 10 scan lines (each of about 20 m length) located along the road. Scan line strikes range between 80 and 140°N. Furthermore, 60 samples have been collected; 42 of them have been useful to calculate ellipticity values.

4.1. Orientation analysis

For the orientation analysis, 261 measurements of foliation, 193 measurements of stretching lineation and corresponding distance (L) from the thrust fault have been recorded. The shear plane, which is parallel to the main thrust fault, dips ca. 20° toward the SW (mean value 227). The stretching lineation displays a dominant SSW plunge (mean value of 197/20), whereas the foliation shows a wider distribution, being dominantly gently dipping to the west (Fig. 4a). Probably due to late gentle folding, both stretching lineation and poles to foliation show a dip variation of ca. 20° around a 290°N trending axis. The restored projection (Fig. 4b) indicates that the stretching lineation is roughly orthogonal to the ESE shear direction shown by sigmoidal foliation and asymmetric (S-shaped) clasts. The geometric relationship between stretching lineation and foliation are effectively displayed by means of the pitch/dip-direction correlation diagram of Carreras, 2001 (Fig. 4c). As the stretching lineation trends close to the strike of thrust plane, the thrust zone can be considered as an oblique foliation/transverse lineation strain facies *sensu* Tikoff and Fossen (1999).

In the following analysis we use the capital letters X, Y, and Z for the orientation of finite strain ellipsoid axes (Ramsay, 1967), whereas the lower case letters x, y, and z indicate the axes of the reference coordinate system, with x parallel to the shear direction and z orthogonal to the shear plane (Fig. 5). Furthermore, we use the letter k_1, k_2 and k_3 to indicate the elongation relative to the pure shear component along the x, y, and z axes of the reference frame, respectively.

In order to obtain correct values of strain gradients, scan line data have been projected along a line orthogonal to the thrust plane, obtaining a final 47 m long section. The angle θ' (*sensu* Ramsay and Huber, 1983) between the shear plane (i.e. the thrust plane) and the XY plane of the finite strain ellipsoid (i.e. foliation) has been projected on the section. The angle θ' has been calculated as the angle between the thrust fault and the foliation. It displays a consistent variation across the shear zone (Fig. 6a), although the data show a degree of spreading that may be considered normal when dealing with natural data. The general trend is shown by the variation of the mean angle θ' (each value being calculated from five measurements) as a function of L (Fig. 6b).

4.2. Finite strain analysis

In order to evaluate ellipticity values along the XZ and YZ principal planes of the finite strain ellipsoid across the shear zone,

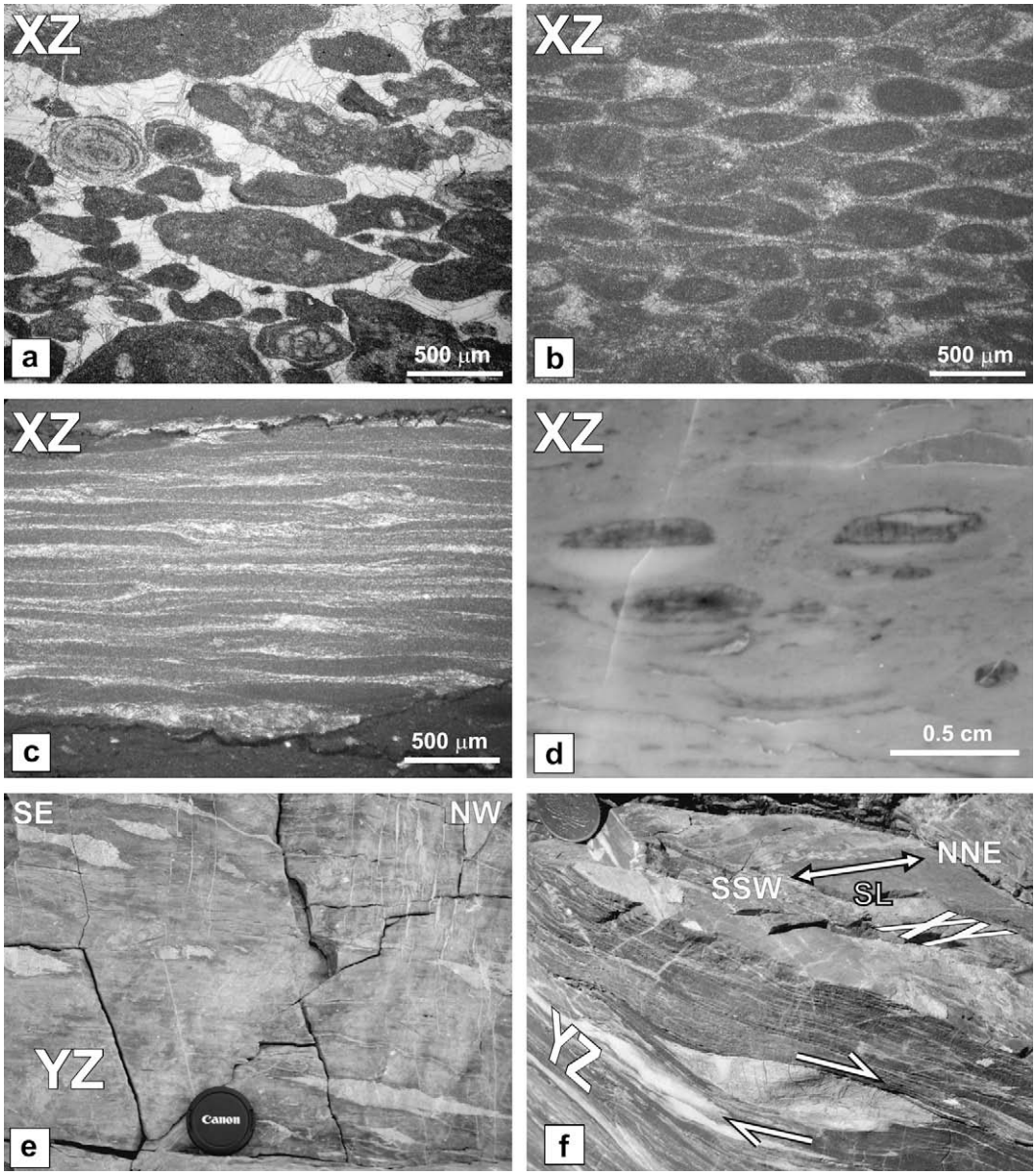

Fig. 3. Thin section microphotographs (a–c), polished slab photographs (d) and outcrop photographs (e, f). (a) Weakly deformed packstone with prevailing sparry cement with respect to micritic objects (*XZ* principal plane, Maratea). (b) Weakly deformed, prevailing micritic, ooidal packstone (*XZ* principal plane, Maratea). (c) Highly deformed micritic ooidal packstone (*XZ* principal plane, Maratea). (d) Large sparry objects (some representing geopetal structures) embedded in a micritic matrix (*XZ* principal plane, Maratea). (e) Asymmetric clasts indicating a top-to-the-SE sense of shear (*YZ* principal plane, San Nicola Arcella). (f) Asymmetric clast indicating a top-to-the-ESE sense of shear and stretching lineation indicating SSW–NNE lengthening (Campotenese).

several oncoidal/ooidal/peloidal/intraclast packstones have been analyzed. For each sample, polished slabs and/or thin sections have been prepared parallel to the *XZ* and *YZ* planes. The former has been determined as a plane orthogonal to foliation and containing the stretching lineation; the latter is orthogonal to both foliation and stretching lineation.

For each polished slab or thin section, a picture has been taken and analyzed by Image-J software (http://rbs.info.nih.gov/ij/). Generally the analyzed rocks are formed by relatively large, elliptical or sub-elliptical, mostly micritic objects embedded in a fine-grained matrix formed by micrite or peloids with a sparry cement. Evaluation of object finite strain has been carried out by the R_f/ϕ method (Dunnet, 1969; Ramsay and Huber, 1983), whereas whole-rock finite strain has been obtained using the normalized Fry method (Erslev, 1988). Object (R_o) and rock (R_s) finite strain may show different values, i.e. rock components show different deformation behaviour. In this case, it is possible to estimate the different rheological behaviour by means the viscosity contrast parameter r (Treagus and Treagus, 2002):

$$r = \ln\left(\frac{R_s}{R_o}\right)\frac{(R_o+1)}{(R_o-1)}+1 \quad (1)$$

For $r < 1$ objects are less competent than the surrounding material (in our instance matrix plus cement); on the contrary, for $r > 1$ objects are more competent. However, care must be taken in giving a real meaning to the parameter r, because its value depends on what is actually considered as objects and surrounding materials. In our instance, a large majority of objects are stiffer than matrix, although they may be composed of the same mineral and grain size (for example micrite). On the other hand, both objects and matrix are softer than cement (generally formed by sparry calcite in limestones). The prevalence of one of these components largely

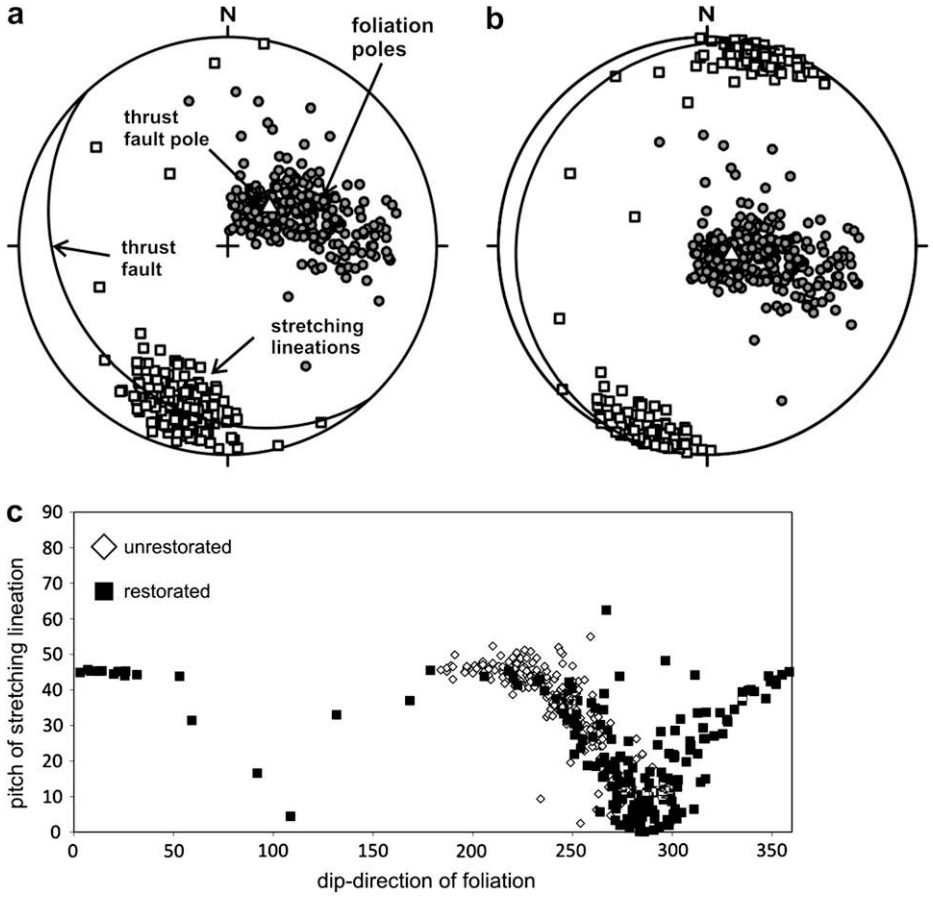

Fig. 4. (a) Orientation data (lower hemisphere, equal area projections) for stretching lineation (white boxes) and foliation (poles to planes; grey circles). (b) Restored orientation data projection (see text). (c) Pitch/dip-direction correlation diagram where both original (white rhombs) and restored configuration (black boxes) have been plotted.

influences viscosity contrast estimates. Furthermore, high values of object concentration remarkably alter the strain ratio for both objects and rock (Treagus and Treagus, 2002; Vitale and Mazzoli, 2005). In the following analysis, object finite strain is used, consistently with the fact that measured foliations and stretching lineations have been determined by means of deformed objects. It is also worth mentioning that, for several samples, an integrated analysis of polished slabs and thin sections has been necessary in order to obtain a correct range of finite strain values. Once mean finite strain values have been measured for the *XZ* and *YZ* principal sections, the ellipticity on the *XY* plane has been calculated as a simple ratio. The three values have been used to evaluate the finite natural logarithmic strain (Ramsay and Huber, 1983):

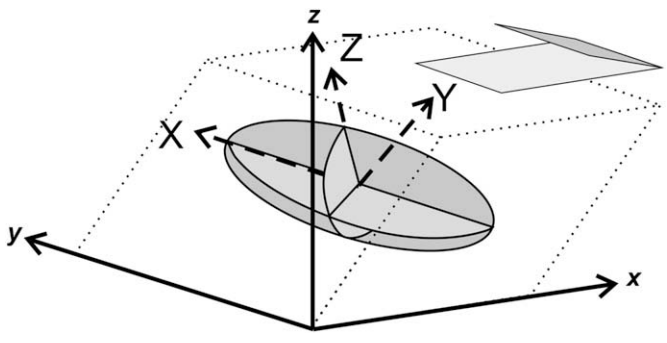

Fig. 5. (a) Block diagram of shear zone showing reference frame used in this study.

$$\varepsilon = \left(\frac{1}{3}\right)^{1/2}\left[(\ln(R_{XZ}))^2+(\ln(R_{YZ}))^2+(\ln(R_{XY}))^2\right]^{1/2} \quad (2)$$

In order to investigate finite strain variations across the shear zone, finite strain parameters (R_{XZ}, R_{YZ}, ε) have been plotted against distance (L) from the thrust plane (Fig. 7a–c); for each distribution, curves of means values and of upper and lower standard deviation boundaries have been plotted. Ellipsoid shape has been analyzed by plotting object finite strain—for *YZ* and *XY* principal sections—in the Ramsay diagram (Fig. 7d). Finally, viscosity contrast values have been calculated by means of eq. (1) for 30 samples and plotted as a function of frequency (Fig. 8).

5. Discussion

The analyzed shear zone is characterized by a severe lengthening orthogonal to the ESE shear direction. This feature is marked by several evidences: (i) stretching lineation is roughly orthogonal to the shear direction as obtained by independent field evidence (Fig. 3e,f); (ii) the stretching lineation trends at a high angle with respect to the general dip-direction of the foliation (Fig. 4a,b); and (iii) the stretching lineation pitch shows low values in the restored configuration (Fig. 4c).

The calculated angle θ' (Fig. 6) shows relatively large variations (up to 20° even on short distances). However, mean values indicate a more consistent trend, oscillating within the range $5^\circ > \theta' > 20^\circ$ at a distance of from 0 to 30 m from the thrust fault. From 40 to 47 m mean θ' values increase, locally exceeding 45°. This trend is better displayed by the best-fit curve, which shows a flat geometry

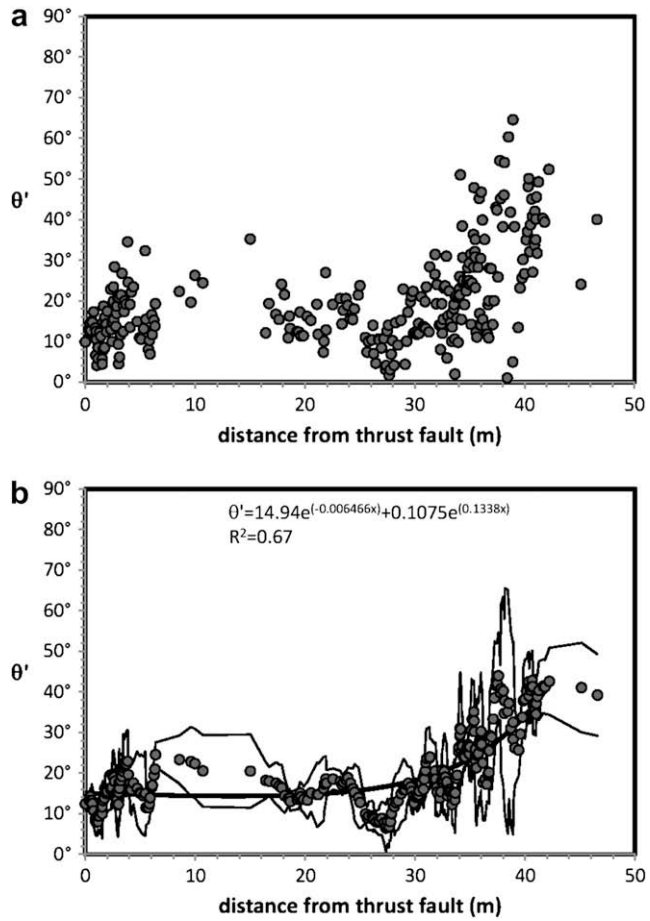

Fig. 6. Diagrams of θ' (a) and mean θ' (b) vs. distance (L) from thrust fault. In b, upper and lower standard deviation boundaries and best-fit curve (sum of two exponentials) are shown.

from 0 to 30 m, constantly increasing farther from the thrust fault. *XZ* and *YZ* finite strain values obtained from deformed objects, as well as the natural logarithmic strain (ε), indicate increasing finite strain approaching the thrust fault (Fig. 7a–c). In particular the mean R_{XZ} finite strain distribution shows a flat-topped shape between 0 and 27 m from the thrust fault, and a negative trend up to 45 m (Fig. 7a). Conversely, the mean R_{YZ} finite strain distribution displays a peaked shape (Fig. 7b). Finally, the natural logarithmic strain distribution shows a broad linear negative trend (Fig. 7c).

Some data scattering, for both θ' and finite strain values, could be related to several factors: (i) a different concentration of objects with respect to matrix and cement, which may significantly influence measured finite strain (Treagus and Treagus, 2002; Vitale and Mazzoli, 2005); (ii) a non-constant rheological behaviour of objects, matrix and cement, as indicated by the calculated viscosity contrast between objects and surrounding material (ranging between 0.25 and 2.75; Fig. 8); and (iii) the occurrence of heterogeneous deformation at various scales. The latter feature is further emphasized by the peak of finite strain located 25–30 m below the thrust fault, rather than at the actual contact (Fig. 7a–c). The natural logarithmic strain (ε) increases in an approximately linear fashion towards the thrust fault (Fig. 7c). Similar linear trends have been observed also in further mylonitic shear zones (Talbot and Sokoutis, 1995). In this study, mylonite types have been distinguished according to observed microstructures and fabrics and not by using matrix concentration with respect to porphyroclasts because the protolith generally has an original micritic grain size. In order to discriminate mylonite types we used intervals of ε of: 0–1 (protomylonites), 1–2.5 (mylonites) and >2.5 (ultramylonites).

The Ramsay diagram (Fig. 7d) shows that most object finite strain ellipsoids fall into the oblate field. Ellipsoids display a moderate oblate shape, plotting close to the plane strain line, up to an R_{YZ} value of ca. 5. For larger strains, ellipsoids rapidly move to strongly oblate shapes. Finite strain ellipsoid distribution in the Ramsay diagram is similar to that obtained for the whole region (Vitale et al., 2007a), thus suggesting a similar finite strain development for the whole shear zone from the areas of Campotenese to that of Maratea (Fig. 1a).

Before attempting to outline the deformation characteristics of the analyzed shear zone, a few broader considerations on the finite strain characterizing the Pollino-Ciagola Unit in the study area need to be carried out. Horizontal strain gradients in the whole zone show a N–S trend (Vitale et al., 2007a) with no deformation along the Pollino chain and Lauria Mountains (Fig. 1a) and highest values in the SW sector (from San Nicola Arcella to Campotenese). This strain pattern is probably related to a combination of two main factors: (i) variable rheology as function of original sedimentary facies distribution (more massive platform carbonates to the NE and slope carbonates including conglomerates to the SW); (ii) different tectonic burial being larger in the SW sector where the Pollino-Ciagola Unit has been overthrusted by the Lungro-Verbicaro Unit, ophiolitic and continental Units, whereas the Pollino chain is exclusively overthrusted by a thinner sheet of ophiolitic material of Liguride Complex (Bonardi et al., 1988). Vertically, the rocks outside the shear zone are essentially undeformed both in the footwall and hanging wall. These features allow one to rule out the presence of bulk pure shear strain components outside the shear zone. The occurrence of a foliation characterized by a mean angle of 45–10° with respect to the thrust fault (Fig. 6) and of finite strain values increasing toward the thrust fault (Fig. 7) suggest heterogeneous simple shear (characterized by top-to-the-ESE sense of shear; Fig. 3e,f). However, the overall oblate strain, the stretching lineation orthogonal to the shear direction and the occurrence of undeformed rocks outside the shear zone all indicate the presence of simultaneous localized pure shear characterized by lengthening ($k_2 > 1$) along the y direction of the reference frame. Furthermore, a variable component of simultaneous localized volume change, with contraction or dilation along the z direction of the coordinate system, cannot be ruled out. In the following analysis, the possible roles of volume change and elongation along the x axis are taken into account by fixing specific values of Δ and k_1, and analyzing how elongation varies along the y axis. In order to model different strain paths as a function of these parameters, six possible combinations of shear zone types are considered. The resulting semi-logarithmic grids of θ' vs. R_{XZ} values (Fig. 9) involve:

(i) $k_1 = 1$ (no pure shear) and $\Delta = 0$ (no volume change) (Fig. 9a);
(ii) $k_1 = 1$ and $\Delta = -0.1$ (10% contraction along the z axis) (Fig. 9b);
(iii) $k_1 = 1$ and $\Delta = +0.1$ (10% positive dilation along the z axis) (Fig. 9c);
(iv) $k_1 = 0.9$ (10% shortening along the x axis) and $\Delta = 0$ (Fig. 9d);
(v) $k_1 = 1.1$ (10% lengthening along the x axis) and $\Delta = 0$ (Fig. 9e);
(vi) $k_1 = 1.1$ (10% lengthening along the x axis) and $\Delta = +0.3$ (30% positive dilation along the z axis) (Fig. 9f).

In all cases, $k_3 = (1 + \Delta)/k_1 k_2$.

These models involve general shear with simultaneous localized simple shear (with the x axis parallel to the shear direction) and variable components of pure shear and volume change (with contraction or dilation along the z axis). The strain matrix describing these configurations is (Fossen and Tikoff, 1993):

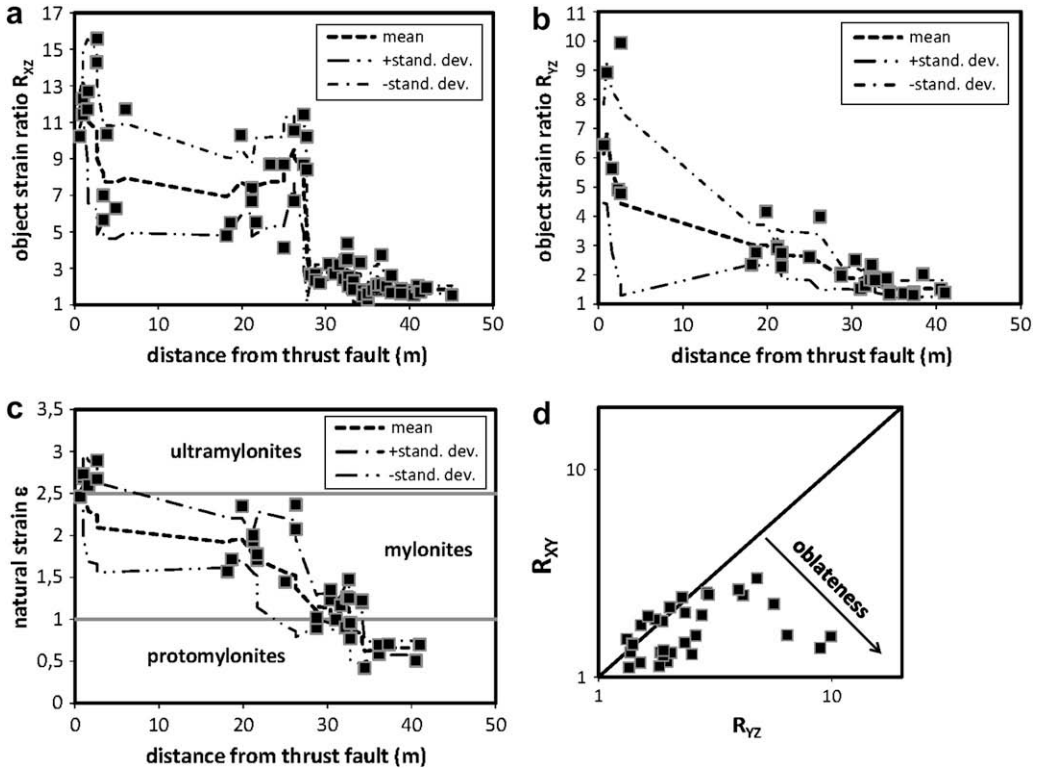

Fig. 7. Diagrams of finite strain vs. distance (L) from thrust fault. (a) R_{XZ} plot. (b) R_{YZ} plot. (c) Natural logarithmic strain (ε) plot. (d) Ramsay diagram of object finite strain ellipsoids.

$$A = \begin{bmatrix} k_1 & 0 & \Gamma \\ 0 & k_2 & 0 \\ 0 & 0 & k_3 \end{bmatrix} \quad \Gamma = \frac{\gamma(k_1 - k_3)}{\ln\left(\frac{k_1}{k_3}\right)} \tag{3}$$

The angle θ' and finite strain (R_{XZ}) values have been obtained by means of the best-fit equations plotted in Figs. 6b and 7a, respectively. It is worth noting that the data points in Fig. 9 do not lie along a strain path characterized by constant values of elongation along y axis (k_2). Rather, they plot along a complex path, indicating that this quantity varies across the shear zone, consistently with the pure shear component being localized within the shear zone. The six combinations represent few examples of an infinite range of possible deformation types. However, it is possible to restrict such a range by discarding those models involving points falling in the $k_2 < 1$ field, such as those characterized by contraction along the z axis (Fig. 9b) or lengthening along the x axis (Fig. 9e), unless this latter is compensated by dilation along the z axis (Fig. 9f). In all the modelled cases, the elongation along the y axis reaches large values ($k_2 > 1$) with a rapid increase in the first part of the deformation path ($1 < R_{XZ} < 5$) and a constant value for the second sector ($R_{XZ} > 5$). On the other hand, in order to maintain the elongation along the y axis within realistic values (i.e. k_2 not exceeding a value of 3), (i) the component of volume change along the z axis cannot reach very large values (Fig. 9c), and (ii) the component of lengthening along the x axis cannot reach very low values (Fig. 9d). By assuming that the finite strain along the y direction (i.e. orthogonal to the shear direction) is mainly due to the pure shear component, and that the finite strain along the x direction (shear direction) is mainly produced by the simple shear component, the finite strain profiles across the shear zone may be considered as essentially related to the pure shear and simple shear components on the xz and yz planes, respectively. Therefore, the diagrams in Fig. 7 show how the finite strain related to simple shear decreases away from the thrust fault, whereas the finite strain related to the pure shear component holds constant along the y axis and subsequently decreases in an abrupt fashion.

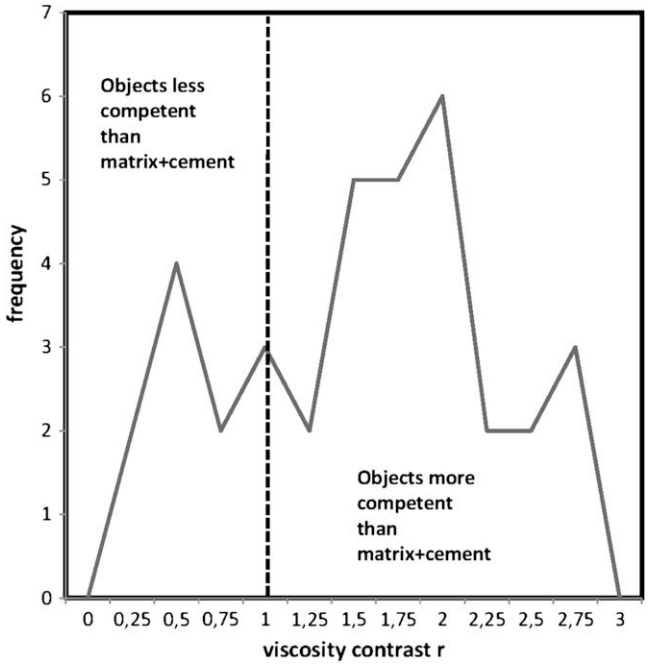

Fig. 8. Histogram of viscosity contrast frequency.

Variable values of elongation across the shear zone, along the y direction, indicate heterogeneous deformation, with low values characterizing weakly deformed rocks and high values occurring in intensely deformed ones. This characteristic implies a 'cream cake effect' (Ramsay and Huber, 1987, p. 611), with extruded material along the y direction (lateral extrusion of Jones et al., 1997). In our instance, an asymmetric extrusion is envisaged (Fig. 10). This is

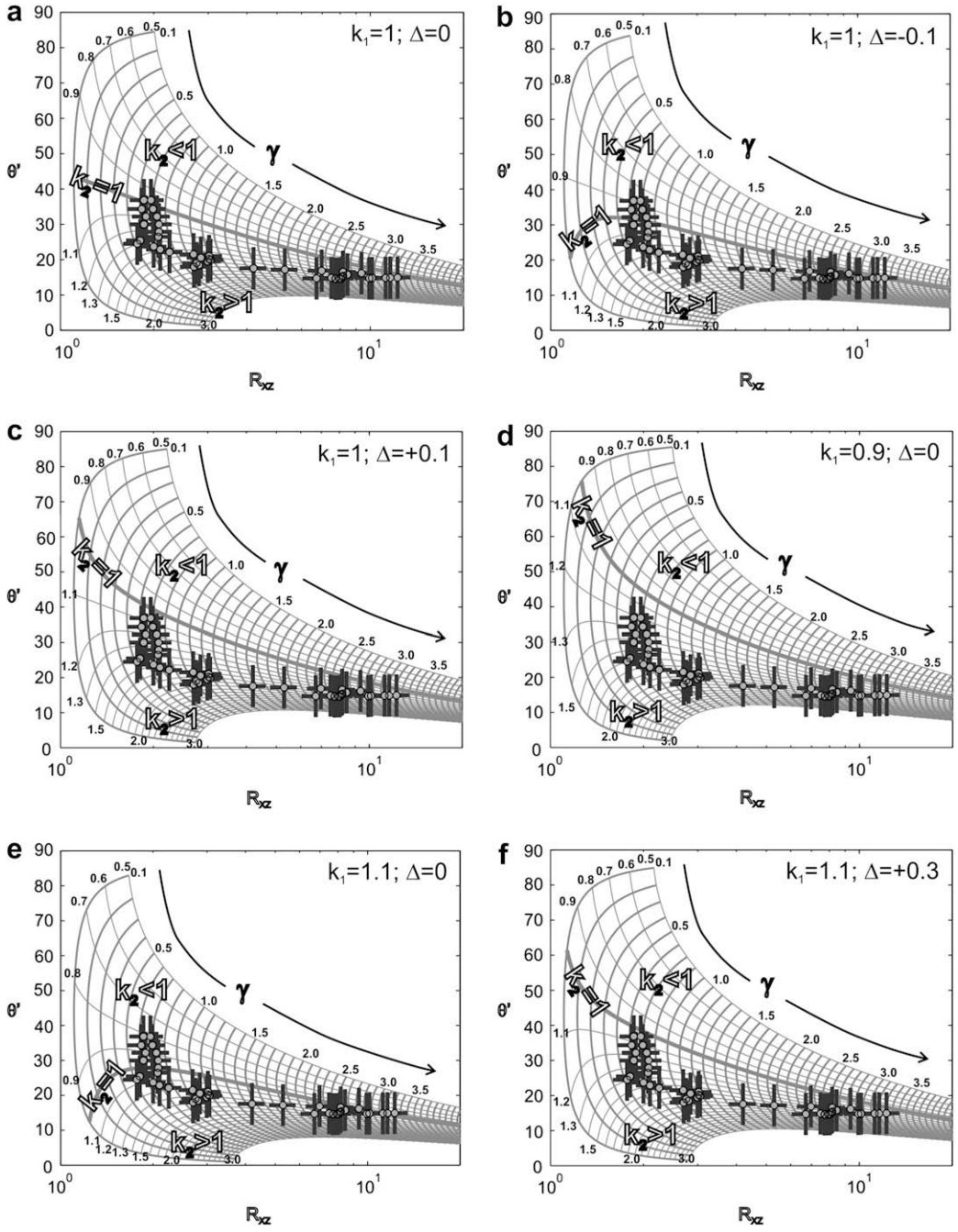

Fig. 9. Mean θ' vs. object finite strain R_{XZ} values plotted on six finite strain grid configurations (a–f).

consistent with the occurrence of essentially undeformed rocks in the NE sector of the study area, which is characterized by extensive outcrop of a several-kilometre-thick succession of platform carbonates (Fig. 1a). These massive rocks would have acted as a rigid buttress with respect to the NNE–SSW oriented stretching associated with the pure shear component of the deformation (orthogonal to the shear direction), triggering southward extrusion. The latter process would be also compatible with the accommodation space being provided for the extruded material along the present-day Tyrrhenian Sea margin.

By considering a minimum hanging wall displacement of about 40 km (Fig. 10) and a shear zone thickness of ca. 50 m, a minimum shear strain of $\gamma = 800$ is obtained. This value is 216 times larger the maximum shear strain (ca. $\gamma = 3.7$) measured from calcareous mylonites. This suggests that most of the thrust fault slip has been accommodated by brittle displacement along the thrust surface itself ('discontinuous strain profile'; Scholz, 1990). Furthermore, a significant amount of ductile strain may have been accumulated in the thin layer of pelites located immediately in the footwall to the thrust fault.

6. Conclusions

The analyzed shear zone is characterized by heterogeneous deformation with increasing finite strain approaching the main thrust fault (Fig. 7c). The overall deformation includes simple shear—with a top-to-the-ESE shear sense—and a localized pure shear component characterized by lengthening orthogonal to the

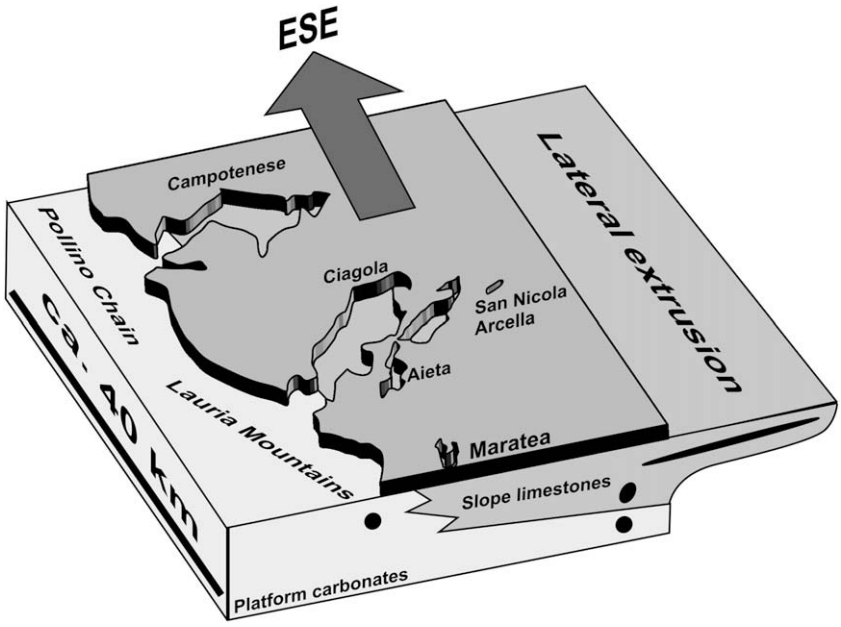

Fig. 10. Cartoon showing heterogeneous ductile shear zone involving asymmetric lateral extrusion in the footwall to the major regional thrust (see text). The vertical dimension is not to scale.

shear direction. It is not possible to rule out a volume change component, as well as a possible pure shear component characterized by extension along the shear direction. In any case, their contribution, if existent, may only be minor with respect to the first two. The stretching lineation is generally orthogonal to the shear direction (Fig. 4), whereas the foliation forms an angle with the thrust fault ranging from 45 to 10° (Fig. 6). These characteristics indicate an oblique foliation/transverse lineation strain facies (Tikoff and Fossen, 1999). The 47 m thick shear zone is characterized by a finite strain profile showing, for the *XZ* principal section of the finite strain ellipsoid, a flat-topped shape for the first 27 m beneath thrust fault. There, R_{XZ} attains relatively large values, abruptly decreasing for larger distances from the thrust plane (Fig. 7a). Conversely, the finite strain profile for the *YZ* principal plane describes a peaked path, showing steadily decreasing intensity with distance from the thrust fault (Fig. 7b). Most of the finite strain ellipsoids fall into the oblate field, being characterized by increasing flattening as a function of finite strain (Fig. 7d). In all the models proposed to unravel the possible combinations of deformation types characterizing the shear zone (Fig. 9), the elongation orthogonal to the shear direction shows a variable intensity across the shear zone, indicating that the pure shear component is localized. The strain compatibility problem between different deformed volumes is overcome by an envisaged asymmetric southward lateral extrusion (Fig. 10). This process is consistent with (i) measured horizontal strain gradients, (ii) the occurrence of accommodation space along the present day Tyrrhenian extensional margin, and (iii) stratigraphic facies distribution, the latter being characterized by the occurrence of massive platform carbonates in the NE sector of the study area.

Acknowledgements

We thank G. D'Andrea, M. Russo and J. White for their cooperation during fieldwork and helpful discussions. The paper greatly benefited from thorough and constructive reviews by P. Hudleston and an anonymous reviewer, as well as associate editor J. Hippertt. Financial support from MIUR—PRIN 2005 (Resp. S. Mazzoli, Coord. G. Cello) is gratefully acknowledged.

References

Baird, G.B., Hudleston, P.J., 2007. Modeling the influence of tectonic extrusion and volume loss on the geometry, displacement, vorticity, and strain compatibility of ductile shear zones. Journal of Structural Geology 29, 1665–1678.
Bonardi, G., Amore, F.O., Ciampo, G., de Capoa, P., Miconnet, P., Perrone, V., 1988. Il Complesso Liguride Auct.: stato delle conoscenze e problemi aperti sulla sua evoluzione pre-appenninica ed i suoi rapporti con l'Arco Calabro. Memorie della Società Geologica Italiana 41, 17–35.
Carreras, J., 2001. Zooming on Northern Cap de Creus shear zones. Journal of Structural Geology 23, 1457–1486.
Dunnet, D., 1969. A technique of finite strain analysis using elliptical particles. Tectonophysics 7, 117–136.
Erslev, E.A., 1988. Normalized center-to-center strain analysis of packed aggregates. Journal of Structural Geology 10, 201–209.
Fossen, H., Tikoff, B., 1993. The deformation matrix for simultaneous simple shearing, pure shearing and volume change, and its application to transpression-transtension tectonics. Journal of Structural Geology 15, 413–422.
Fossen, H., Tikoff, B., 1997. Forward modeling of non-steady-state deformations and the 'minimum strain path'. Journal of Structural Geology 7, 978–996.
Horsman, E., Tikoff, B., 2007. Constraints on deformation path from finite strain gradients. Journal of Structural Geology of London 29, 256–272.
Hull, J., 1988. Thickness-displacement relationships for deformation zones. Journal of Structural Geology 10, 431–435.
Iannace, A., Vitale, S., D'Errico, M., Mazzoli, S., Di Staso, A., Macaione, E., Messina, A., Reddy, S.M., Somma, R., Zamparelli, V., Zattin, M., Bonardi, G., 2007. The carbonate tectonic units of northern Calabria (Italy): A record of Apulian paleomargin evolution and Miocene convergence, continental crust subduction, and exhumation of HP-LT rocks. Journal of the Geological Society of London 164, 1165–1186.
Jones, R.R., Holdsworth, R.E., Bailey, W., 1997. Lateral extrusion in transpression zones: the importance of boundary conditions. Journal of Structural Geology 19, 1201–1217.
Means, W.D., 1995. Shear zones and rock history. Tectonophysics 247, 157–160.
Ramsay, J.G., 1967. Folding and Fracturing of Rocks. McGraw-Hill, New York.
Ramsay, J.G., Graham, R.H., 1970. Strain variation in shear belts. Canadian Journal of Earth Sciences 7, 786–813.
Ramsay, J.G., Huber, M., 1983. The Techniques of Modern Structural Geology. In: Strain Analysis, Volume I. Academic Press, London.
Ramsay, J.G., Huber, M., 1987. The Techniques of Modern Structural Geology. In: Folds and Fractures, Volume II. Academic Press, London.
Ring, U., 1998. Volume strain, strain type and flow path in a narrow shear zone. Geologische Rundschau 86, 786–801.
Scholz, C.H., 1990. The Mechanics of Earthquakes and Faulting. University Press, Cambridge.
Srivastava, H.B., Hudleston, P., Earley III, D., 1995. Strain and possible volume loss in a high-grade ductile shear zone. Journal of Structural Geology 17, 1217–1231.
Talbot, C., Sokoutis, D., 1995. Strain ellipsoids from incompetent dykes: application to volume loss during mylonitization in the Singö gneiss zone, central Sweden. Journal of Structural Geology 17, 927–948.
Tikoff, B., Fossen, H., 1999. Three-dimensional reference deformations and strain facies. Journal of Structural Geology 21, 1497–1512.

Treagus, S.H., Treagus, J.E., 2002. Studies of strain and rheology of conglomerates. Journal of Structural Geology 24, 1541–1567.

Vitale, S., Mazzoli, S., 2005. Influence of object concentration on finite strain and effective viscosity contrast: Insights from naturally deformed packstones. Journal of Structural Geology 27, 2135–2149.

Vitale, S., Mazzoli, S., 2008. Heterogeneous shear zone evolution: the role of shear strain hardening/softening. Journal of Structural Geology 30, 1383–1395, doi:10.1016/j.jsg.2008.07.006.

Vitale, S., Iannace, A., Mazzoli, S., 2007a. Strain variations within a major carbonate thrust sheet of the Apennine collisional belt, northern Calabria, southern Italy. In: Ries, A.C., Butler, R.W.H., Graham, R.H. (Eds.), Deformation of the Continental Crust: The Legacy of Mike Coward. Geological Society, vol. 272. Special Publications, London, pp. 145–156.

Vitale, S., White, J.C., Iannace, A., Mazzoli, S., 2007b. Ductile strain partitioning in micritic limestones, Calabria, Italy: the roles and mechanisms of intracrystalline and intercrystalline deformation. Canadian Journal of Earth Sciences 44, 1587–1602.